

Fast and Robust T_1 Mapping Based on a 3D Dual-Echo UTE Sequence (PETALUTE) for SPION Biodistribution Assessment

Author

Zhen Jiang¹, Stephen Sawiak^{2,3}, Alexandra Lipka^{1,5,6}, Xin Shen⁷, Uzay Emir⁸, Ali Özen⁹, Mark Chiew^{10,11,12}, Justin Geise¹, Joseph Speth¹, Deng-Yuan Chang¹, Jessica Veenstra¹, Mitchell Gabalski¹³, Luis Solorio¹³, Gregory Tamer Jr.¹³, Matthew Scarpelli¹

¹School of Health Sciences, College of Health and Human Sciences, Purdue University, West Lafayette, IN, United States, ²Department of Physiology, Development, and Neuroscience, University of Cambridge, Cambridge, United Kingdom, ³Department of Clinical Neurosciences, Wolfson Brain Imaging Centre, Cambridge, United Kingdom, ⁵College of Engineering, Purdue University, West Lafayette, IN, United States, ⁶Division of Medical Physics in Radiology, German Cancer Research Center (DKFZ), Heidelberg, Germany, ⁷Department of Radiology, University of California San Diego, San Diego, CA, United States, ⁸Department of Radiology, University of North Carolina at Chapel Hill, Chapel Hill, NC, United States, ⁹Department of Radiology, Medical Physics, Medical Center-University of Freiburg, Faculty of Medicine, University of Freiburg, Freiburg, Germany, ¹⁰Nuffield Department of Clinical Neurosciences, University of Oxford, Oxford, United Kingdom, ¹¹Physical Sciences Platform, Sunnybrook Research Institute, Toronto, ON, Canada, ¹²Department of Medical Biophysics, University of Toronto, Toronto, ON, Canada, ¹³Weldon School of Biomedical Engineering, Purdue University, West Lafayette, IN, United States

Abstract

Background

Superparamagnetic iron oxide nanoparticles (SPIONs), such as ferumoxytol, are promising theranostic agents that can be assessed with MRI. Relaxation time mapping can provide reproducible and quantitative biomarkers of SPION distribution, suitable for longitudinal and cross-individual studies. However, conventional approaches suffer from strong susceptibility artifacts, long echo times (TE), and prolonged scan times, which limit the accurate quantification of SPION biodistribution.

Purpose

To address the limitations of conventional approaches, this study aimed to develop a fast, B_1 -corrected T_1 mapping protocol based on PETALUTE (a 3D dual-echo ultrashort echo time MRI sequence with rosette k-space trajectory) using a variable flip-angle (VFA) acquisition for quantitative mapping of ferumoxytol distribution.

Method

Agarose phantoms containing 0-5000 ppm ferumoxytol were scanned on a preclinical 7T MRI system using PETALUTE and a vendor-supplied T_1 mapping (RARE-VTR). PETALUTE T_1 maps were computed from two VFA acquisitions (4° and 20°). Mean R_1 values were correlated with ferumoxytol concentration to assess the method's reliability. For in vivo feasibility testing, mice bearing 4T1 mammary tumors and flank tumors were assigned to the control ($n = 1$) or ferumoxytol-injected group ($n = 2$; 40 mg/kg i.v.). Abdominal MRI scans were performed 24 hours post-injection with both PETALUTE and RARE-VTR. Regions of interest in the thigh muscle, mammary tumors, and flank tumors were analyzed to compare the estimated T_1 and R_1 values obtained with both methods.

Results

In the phantom study, PETALUTE showed positive contrast for ferumoxytol at all concentrations except the highest concentration (5000 ppm), whereas the conventional RARE-VTR could not produce a positive contrast. For PETALUTE, there was a significant linear correlation between R_1 and ferumoxytol concentration ($R = 0.975$, $p < 0.01$), while RARE-VTR showed no significant correlation ($R = 0.672$, $p = 0.144$). In vivo, PETALUTE provided high-resolution, non-gated, whole-abdominal images with short acquisition times (4 minutes 19 seconds). In ferumoxytol-injected mice, flank tumors exhibited T_1 shortening, consistent with the expected iron accumulation. The dual-echo capabilities of PETALUTE facilitated observation of elevated T_1 with preserved T_2^* -weighted signal in one of the mammary tumors.

Conclusions

The proposed PETALUTE-based T_1 mapping enables fast, quantitative, and positive-contrast ferumoxytol imaging with higher spatial coverage and more stable measurements across a wider concentration range than conventional RARE-VTR T_1 mapping.

Introduction

Nanoparticles (NPs) are a powerful platform for precision cancer therapy, enhancing the therapeutic index by concentrating agents in tumors while minimizing off-target exposure^{1, 2}. In practice, NP uptake varies widely across patients and tumor types^{3, 4}. This variability makes the effective dose unpredictable, complicating treatment planning and clinical translation.

Theranostic NPs, which combine therapeutic and imaging functions in a single platform, have therefore been used for the simultaneous treatment and visualization of NP delivery^{5, 6, 7}.

However, a noninvasive imaging modality is still required to confirm target engagement and enable personalized, response-adaptive dosing strategies⁴.

Magnetic resonance imaging (MRI) is well-suited for theranostic NP tracking. It is non-ionizing, widely available, and offers high spatial resolution with excellent soft-tissue contrast.

Superparamagnetic iron oxide nanoparticles (SPIONs), such as ferumoxytol, are MRI-visible theranostic NPs owing to their intrinsic physical properties⁸. They shorten both the transverse (T_2/T_2^*) and longitudinal relaxation times (T_1)^{9, 10, 11}, appearing brighter on T_1 -weighted MRI images and darker on T_2/T_2^* -weighted MRI images.

However, MRI signal intensity alone is not a reliable quantitative indicator of SPION, as it is inherently arbitrary. Quantitative MRI (qMRI) is a more reliable approach that offers reproducible measurements grounded in physics models of the MR signal, derived from multiple images acquired with varied parameters to capture tissue-specific properties¹². In particular, T_1 and T_2/T_2^* mapping yield voxel-wise parametric maps that encode quantitative relaxation values, reflecting tissue composition and the local magnetic environment^{13, 14, 15, 16}. These relaxation mapping techniques have also been investigated for assessing SPION biodistribution^{9, 17, 18, 19, 20, 21}, although several challenges remain in their application to SPION imaging.

T_2/T_2^* mapping is sensitive to SPIONs, but its accuracy and efficiency decline as concentration increases⁹. At high concentrations, strong susceptibility artifacts cause the blooming effect and signal voids, degrading spatial localization and quantitative assessment²⁰. In contrast, T_1 mapping is more robust to susceptibility artifacts and can offer a higher signal-to-noise ratio (SNR) than T_2 mapping²⁰, but it still has essential limitations in SPION imaging. First, conventional T_1 mappings, such as Inversion Recovery Spin-Echo (IR-SE) and Rapid Acquisition with Relaxation Enhancement with Variable TR (RARE-VTR), utilize echo times (TE) longer than the ultrashort T_2 of SPION-rich regions, resulting in T_2 -related signal loss and inaccurate T_1 calculations. In addition, a long repetition time (TR) is usually required to achieve complete relaxation for T_1 mapping, increasing susceptibility to motion artifacts and hindering clinical feasibility.

Ultra-short echo time (UTE) MRI is a promising technique to address the challenges described above^{21, 22}. It can capture rapidly decaying signals and provide positive T_1 contrast for SPIONs²³. However, the UTE MRI signal can be challenging to interpret *in vivo* because the short- T_2^* signal from SPION is often masked by the long- T_2^* signal from water and fat (e.g., necrotic tissue)^{22, 24} or confounded by other short- T_2^* components such as calcification or

hemorrhagic byproducts²⁵. Dual-echo UTE methods have been developed to separate short- and long- T_2^* components, but, to our knowledge, their applications have mostly been tissue-specific rather than focused on SPION tracking^{26, 27}. A dual-echo UTE T_1 mapping approach needs to be adapted for SPION monitoring.

To achieve this, we propose a T_1 mapping protocol based on PETALUTE, a 3D dual-echo UTE MRI sequence with a rosette k-space trajectory^{28, 29}. PETALUTE acquires two echoes with ultrashort and longer TEs in a single acquisition. The dual-echo design, combined with an efficient sampling pattern that minimizes coherent undersampling artifacts, is particularly advantageous for SPION imaging. Furthermore, PETALUTE offers 3D high spatial resolution with a short acquisition time, which facilitates its clinical translation.

In this study, we developed and evaluated the performance of the PETALUTE T_1 mapping protocol for ferumoxytol quantification in vitro and in vivo. By combining PETALUTE with variable-flip-angle (VFA) acquisition³⁰ and B_1 map correction³¹, we generated quantitative T_1 maps for ferumoxytol assessment. We hypothesize that PETALUTE will maintain a positive contrast of ferumoxytol while reducing susceptibility artifacts, even at high concentrations, and will enable acquisition of two contrasts with different TEs. To test this hypothesis, we compared PETALUTE T_1 maps with conventional RARE-VTR T_1 maps across a range of ferumoxytol concentrations in phantoms. In addition, we assessed the in vivo feasibility of using PETALUTE T_1 maps for evaluating ferumoxytol in a dual-tumor mouse model.

Materials and Methods

T_1 Map Calculation

PETALUTE T_1 mapping workflow is illustrated in **Figure 1**. We first generated apparent T_1 maps using PETALUTE first echoes from the VFA acquisitions (4° , i.e., the Ernst angle, and 20°) using **Equation 1**, based on the spoiled gradient-echo signal equation^{30, 32}.

$$T_{1,app} = 2 \cdot TR \cdot \frac{S_1/\alpha_1 - S_2/\alpha_2}{S_2 \cdot \alpha_2 - S_1 \cdot \alpha_1} \quad \text{Equation 1}$$

$T_{1,app}$ represents the apparent T_1 value; and S_1, S_2 are signal intensities from PETALUTE first echoes acquired with flip angles of 4° (α_1) and 20° (α_2), respectively.

Under a fully relaxed condition ($TR \geq 5T_1$), the ratio between the two signal intensities, r , can be written as³¹

$$r = S_{1,\infty}/S_{2,\infty} = \sin\alpha_1/\sin\alpha_2 \quad \text{Equation 2}$$

The PETALUTE sequence, however, uses a very short TR that prevents complete longitudinal relaxation. Therefore, a short-TR correction was applied to estimate the fully relaxed signals³³.

The actual flip-angle $\alpha_{1,act}$ was then calculated by combining **Equation 2** with the trigonometric multi-angle formula:

$$\alpha_{1,act} = \sqrt{5 + \frac{4}{r}} \quad \text{Equation 3}$$

The corresponding voxel-wise B_1 map was then computed as the ratio of the actual flip-angle to nominal flip-angle (**Equation 4**).

$$B_1(x, y, z) = \alpha_{1,act}(x, y, z)/\alpha_1 \quad \text{Equation 4}$$

Finally, the B_1 map was applied to correct the apparent T_1 map, producing the PETALUTE T_1 map (**Equation 5**).

$$T_1(x, y, z) = T_{1,app}(x, y, z) \cdot b1^{-2}(x, y, z) \quad \text{Equation 5}$$

The RARE-VTR T_1 maps were computed by voxel-wise nonlinear least-squares fitting of a mono-exponential recovery model (**Equation 6**) to the multi-TR data.

$$S(TR) = S_0(1 - e^{-TR/T_1}) \quad \text{Equation 6}$$

Imaging Protocol and Reconstruction

Imaging protocol included vendor-provided RARE-VTR, Multi-Echo Gradient-Echo (MGE) and the proposed PETALUTE sequences. Parameters are summarized in **Table 1**. All scans were performed on a 7T horizontal-bore small animal MRI system (BioSpec 70/30; Bruker Instruments; maximum gradient strength: 660 mT/m; maximum slew rate: 4570 T/m/s).

RARE-VTR and MGE images were reconstructed on-scanner automatically using Bruker ParaVision 6.0.1. PETALUTE data were processed in MATLAB (202Xa, MathWorks, USA). The nonuniform fast Fourier transform (NUFFT) method was used to reconstruct the PETALUTE images using BART (Berkeley Advanced Reconstruction Toolbox; nufft for NUFFT reconstruction, ecalib for ESPIRiT coil-sensitivity estimation, and pics for iterative CS-SENSE) and MIRT (Michigan Image Reconstruction Toolbox; Gmri and ir_mri_density_comp to define the non-Cartesian encoding operator and density-compensation weights).

Phantom Study

A 1 mL 0 ppm phantom (4.2% agarose) and six ferumoxytol (Feraheme, AMAG Pharmaceuticals) phantoms at targeted concentrations of 100, 250, 750, 1000, 1250, and 5000 ppm were prepared. Ferumoxytol was mixed into 4.2% agarose under heating and continuous stirring. Concentrations were verified by X-ray fluorescence. The ferumoxytol-agarose mixture was allowed to cool at room temperature until it gelled. A piece of the mixture was then scooped out and coated with a thin glue to keep it intact. Finally, the piece was embedded in a 1 mL microcentrifuge tube pre-filled with 4.2% agarose to form the ferumoxytol phantom. Embedding the small piece of ferumoxytol-infused agarose within 4.2% agarose created a compact phantom in which the ferumoxytol exhibits positive contrast relative to the surrounding agarose and remains compatible with the size constraints of the MRI coil. After cooling to room temperature, all the phantoms were stored in a refrigerated environment. They were allowed to warm at room temperature for two hours before scanning.

All phantoms were scanned using a 23-mm-diameter Tx/Rx 1H RF volume coil (Bruker BioSpin, Ettlingen, Germany). PETALUTE images were acquired with a total of 9,216 petals, each petal containing 206 sampling points with 103 sampling points per echo. RARE-VTR and PETALUTE T_1 maps were calculated as previously described. Regions of interest (ROIs) were defined in 3D Slicer³⁴ around the ferumoxytol. For each concentration, the mean and standard deviation of T_1 and R_1 were calculated within the ROI.

The relaxation rate R_1 , defined as the reciprocal of T_1 , has an approximately linear relationship with the concentration of ferumoxytol, as described in **Equation 7**¹⁹.

$$R_1(C) = R_{1,0} + a \cdot C \quad \text{Equation 7}$$

Where C is the ferumoxytol concentration (ppm), $R_{1,0}$ is the intrinsic R_1 of the agarose solution (s^{-1}), and a is the slope ($ppm^{-1} s^{-1}$).

A calibration curve was established by linear regression analysis of R_1 and ferumoxytol concentration.

In vivo Feasibility Study

Female BALB/c mice (8-10 weeks old) were obtained from Envigo (Lafayette, Indiana) and housed in the local facility under pathogen-free conditions. All experiment procedures were reviewed and approved by the local institution in accordance with ARRIVE guidelines.

4T1 cells were obtained from ATCC and cultured in RPMI-1640 medium containing 10% FBS and 1% penicillin/streptomycin. All cultures were incubated at 37°C under humidified conditions with 5% CO₂ and 95% air.

Three female BALB/c mice bearing 4T1 mammary and flank tumors (dual tumor model) were used in this experiment. To establish the model, mice were subcutaneously injected with a single-cell suspension of 1×10^5 4T1 tumor cells in 50 µL of PBS into the fourth right mammary fat (designed as primary tumor), and 5×10^4 4T1 cells in 50 µL of PBS into the left upper thigh (designed as flank tumor). Mice were divided into control (n = 1) and ferumoxytol-injected (n = 2) groups. Fourteen days after tumor implantation, the ferumoxytol group received a single dose of 40 mg/kg ferumoxytol administered via the tail vein.

MRI scans were conducted 24 hours after injection. All mice were scanned using a 7T MRI system with a 40-mm-diameter Tx/Rx 1H RF volume coil (Bruker BioSpin, Ettlingen, Germany), and anesthesia was maintained at 2% isoflurane in oxygen throughout the imaging process. PETALUTE images were acquired using 36,864 petals with 206 sampling points per petal (103 sampling points per echo). RARE-VTR images were also obtained for comparison.

ROIs were manually delineated in the thigh muscle (as a reference region), mammary tumors, and flank tumors using 3D Slicer³⁴, and quantitative analyses were performed in MATLAB. For each ROI, the mean and standard deviation of T₁ and R₁ were calculated from both PETALUTE and RARE-VTR T₁ maps to enable comparative evaluation.

Result

Phantom Study

Figure 2 presents reconstructed images of all phantoms acquired using RARE-VTR and PETALUTE, demonstrating the positive contrast of ferumoxytol produced by the PETALUTE first echo and the negative contrast by the second echo. It should be noted that the PETALUTE images lost some positive contrast for ferumoxytol at a concentration of 5000 ppm. The RARE-VTR images did not have positive contrast at any tested ferumoxytol concentration.

To evaluate the quantitative sensitivity, the relationship between mean R₁ values and ferumoxytol concentration was analyzed (**Figure 3**). A significant positive linear correlation was observed for PETALUTE-based mean R₁ ($R = 0.975$, $p < 0.01$). In contrast, the RARE-VTR-based mean R₁ did not show significant correlation ($R = 0.672$, $p = 0.144$). Additionally, the PETALUTE R₁ standard deviations were lower than those for RARE-VTR, as shown in **Table 2**,

indicating improved precision. The 5000 ppm phantom data were excluded from the linear regression model due to severe susceptibility artifacts in both PETALUTE and RARE-VTR images (**Figure 2**).

In Vivo Feasibility Study

Reconstructed PETALUTE images cover the whole abdominal region and provide visualization of anatomical features (**Figure 4**). Notably, structures such as the kidneys and livers, which were poorly defined in the RARE-VTR images due to a limited field of view, were distinguishable using PETALUTE. In addition, while RARE-VTR images displayed a hypointense region within the flank tumor, PETALUTE showed slightly higher signal intensity near the tumor center (**Figure 5**).

ROIs within the thigh muscle, flank tumors, and mammary tumors allowed the determination of T_1 values from PETALUTE and RARE-VTR. The overall mean T_1 and R_1 values for each mouse and the respective ROI are reported in **Table 3**. For both T_1 mapping methods, muscle tissue mean T_1 values remained relatively stable across mice. For RARE-VTR, the mean muscle T_1 values for the ferumoxytol-injected mice were within 6% of the control mouse T_1 values. For PETALUTE, the mean muscle T_1 values for ferumoxytol-injected mice were within 4% of the control mouse T_1 values.

In the flank tumor, both T_1 mapping methods yielded lower mean T_1 values in ferumoxytol-injected mice than in control mouse. The T_1 reduction in the flank tumor in ferumoxytol-injected mice was approximately 10–12% with RARE-VTR and 4–7% with PETALUTE. In the mammary tumor, T_1 changes differed across the two T_1 mapping methods. With RARE-VTR, both the ferumoxytol-injected mice exhibited an approximately 9–11% T_1 reduction relative to the control mouse. PETALUTE, however, revealed divergent responses: relative to the control mouse (MS47), the mean T_1 increased by approximately 42% in MS48 but decreased by approximately 4% in MS49.

Discussion

We developed a B_1 -corrected PETALUTE-VFA T_1 mapping protocol that enables quantitative, high-resolution imaging of ferumoxytol. This new protocol improved the linearity between R_1 and ferumoxytol concentration, produced positive contrast at high ferumoxytol concentrations, and expanded spatial coverage, thereby overcoming the poor image quality and signal losses that limit conventional T_1 mapping for SPION imaging.

The improved quantitative performance of PETALUTE T_1 mapping in the phantom study is attributed to its ultrashort echo time, which enables signal acquisition from iron before substantial T_2^* -related dephasing occurs. This early acquisition results in higher SNR and reduced variability in estimated T_1 values. Consequently, the protocol delivers more precise quantitative measurements. It establishes a reliable calibration curve for T_1 -based ferumoxytol quantification up to 1250 ppm, whereas the conventional RARE-VTR sequence failed to achieve comparable results. Furthermore, reduced susceptibility effects at lower magnetic field strengths are anticipated to extend the usable linear range of the calibration curve, suggesting that the limits reported here at 7T are likely conservative compared with low-field ferumoxytol quantification methods³⁵.

The in vivo scanning demonstrated the feasibility of using the PETALUTE T_1 mapping protocol to assess ferumoxytol distribution in rodent tumors. Given that no accumulation of ferumoxytol was expected in muscle tissue, the muscle served as a reference region. As expected, we observed minimal differences in T_1 values in this region between the control and ferumoxytol-injected groups, with mean muscle T_1 values within 6% for RARE-VTR and within 4% for PETALUTE relative to the control mouse. In tumors, accumulation of ferumoxytol was expected to lead to T_1 shortening, including decreased T_1 values and increased T_1 -weighted MRI signal intensity. This behavior was observed in the flank tumors of ferumoxytol-injected mice in our study, which exhibited lower T_1 values with both methods and higher intratumoral signal intensity in the PETALUTE first echo. This finding supports the expected preferential accumulation of ferumoxytol within tumor tissue, consistent with prior reports of tumor-specific ferumoxytol uptake that manifests as decreased T_1 values³⁶. The greater T_1 reduction observed with RARE-VTR is likely due to its longer TE (20 ms), which leads to substantial T_2 dephasing in the presence of ferumoxytol. This residual T_2 weighting reduces the effective MRI signal in RARE-VTR images, causing hypointensity and exaggerating the apparent T_1 -shortening effect. In contrast, the ultrashort TE of PETALUTE (0.016 ms) minimizes T_2^* decay, enabling acquisition of an accurate T_1 -weighted signal before substantial dephasing occurs.

However, an unexpected result was observed in the in vivo study. One of the ferumoxytol-injected mice (MS48) exhibited a nearly 42% increase in mean PETALUTE T_1 in the mammary tumor. To investigate this unexpected finding, multimodal images were examined (**Figure 6**). In the MS48 mammary tumor, the combination of T_1 hypointensity and persistent T_2^* signal (indicated by dashed arrow in **Figure 6**) has been reported in previous studies as a marker of tumor necrosis³⁷. These image features are also consistent with an increase in T_1 and T_2^*

values. Although originally reported in a different tumor model rather than in the 4T1 mammary tumor, increases in T_1 and T_2^* are broadly associated with inflammation or necrosis¹⁴. Importantly, the larger tumor volume in the MS48 mammary tumor (MS47: 152 mm³, MS48: 210 mm³, MS49: 189 mm³) likely promoted necrosis, which dominated the MR signal response³⁷. Based on the phantom study (**Figure 2**), ferumoxytol accumulation is anticipated to produce hyperintensity on the PETALUTE first echo and hypointensity on the second echo. Therefore, the hyperintensity region observed in the PETALUTE second echo of MS48 (**Figure 6**) is not consistent with ferumoxytol accumulation and is more plausibly attributed to a long T_2 component, such as fluid-like necrosis. Overall, these observations suggest that the hyperintensity observed in the MS48 tumor across both PETALUTE echoes likely reflects a mixture of necrotic and iron-rich tissue. The resulting PETALUTE T_1 map revealed elevated T_1 values in these potential necrosis-dominated regions. Interestingly, the RARE-VTR T_1 map was not sensitive to these effects (**Figure 6**). Similar intratumoral hyperintensity was also observed in both PETALUTE echoes of MS49, though without measurable T_1 elevation. This might arise from mild or early-stage necrosis, which was insufficient to alter the overall MR signal behavior. Taken together, these findings highlight PETALUTE's ability to capture biological information that may be missed with conventional sequences. Tumor necrosis is a well-established prognostic indicator, and a noninvasive means to measure it would be valuable. Further histological studies are required to confirm this interpretation.

This study has several limitations that should be acknowledged. First, PETALUTE images appear slightly blurrier than those acquired with RARE-VTR (**Figure 5**). This is primarily because we deliberately use a high undersampling factor together with a CS-SENSE reconstruction to enable faster, non-gated whole abdominal T_1 mapping. For the target nominal resolution (matrix = 256 × 256 × 256, r = 128), the Nyquist criterion corresponds to approximately $4\pi \times r^2$ petals ($4\pi \times 128^2 \approx 2.1 \times 10^5$). In comparison, our protocol uses 36,846, which is 18% of the Nyquist sampling density. This level of undersampling reduces image sharpness and fine edge detail, leading to some loss of anatomic definition relative to RARE-VTR. However, previous work has shown that PETALUTE T_1 estimates remain stable even at higher undersampling level (18,192 petals), so substantial degradation of T_1 values is not expected at the sampling density used here³⁸. If higher anatomical clarity is desired, the protocol can be adapted by increasing the sampling density. Second, although the PETALUTE T_1 mapping approach extends the reliable quantitative range of ferumoxytol concentrations, it remains limited at very high concentrations. At 5000 ppm (5 mg/mL), the susceptibility of ferumoxytol at 7T results in a local frequency shift of approximately 20 kHz and an estimated T_2^*

of about 0.01 ms³⁹. These large off-resonance effects and extremely short T₂* lead to considerable signal attenuation and k-space misregistration that severely degrade T₁ mapping accuracy.

Future studies will focus on validating *in vivo* findings with histological evidence. Further evaluation of PETALUTE's performance will also be carried out using simulations to understand how varying SPION concentration, off-resonance, and T₂* shortening affect T₁ mapping precision.

Conclusion

In summary, the PETALUTE T₁ mapping protocol provides more reliable ferumoxytol quantification compared with RARE-VTR. Uniquely, this protocol enables high-resolution, non-gated whole-abdominal images and dual-echo imaging within a single scan. This multimodal capability makes PETALUTE particularly valuable for monitoring treatment with SPION-based therapies.

Acknowledgments

This work was supported by NIH grant 1R01NS131160. Additional support from Eli Lilly and Company is gratefully acknowledged. The authors also gratefully acknowledge the support from the Institute for Cancer Research, NIH grant P30 CA023168.

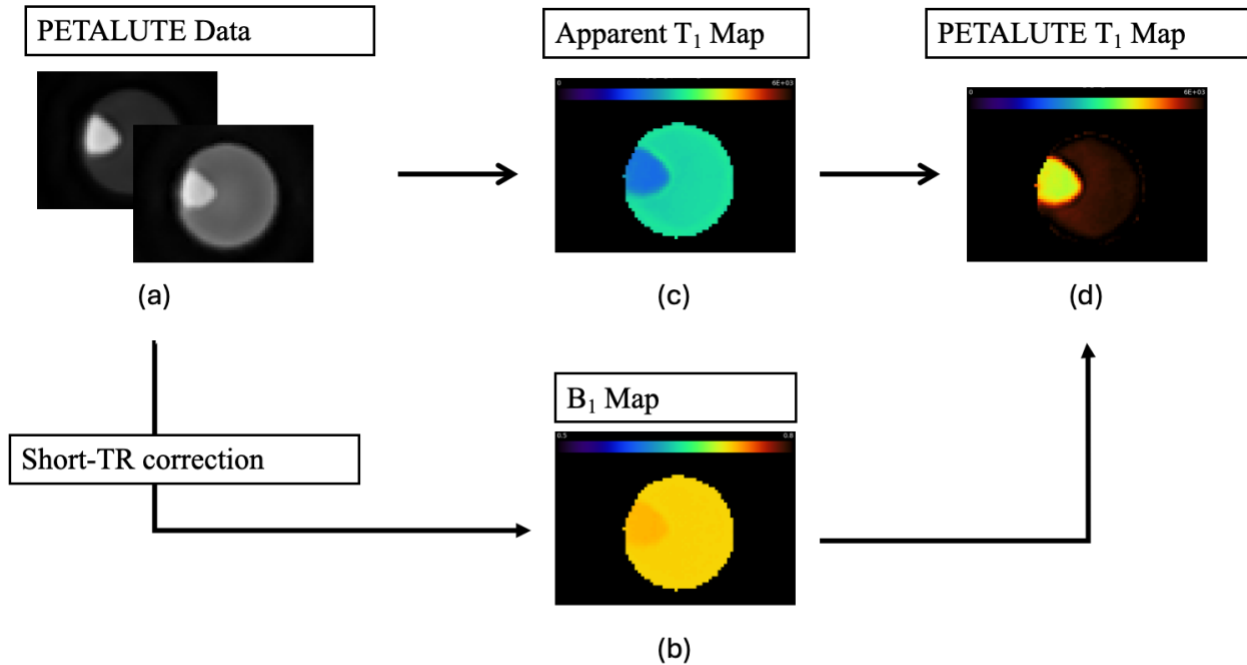


Figure 1. (a) PETALUTE image reconstructed using nonuniform fast Fourier transform method. (b) B_1 map generated by the variable flip angle method with short-TR correction and smoothed using a Gaussian filter with $\sigma = 3$; color bar range from 0.5 to 0.8. (c) Apparent T_1 map generated using the two flip-angle PETALUTE images; color bar range from 0 to 6000 ms. (d) PETALUTE T_1 map derived from the apparent T_1 map corrected using the B_1 map; color bar range from 0 to 6000 ms.

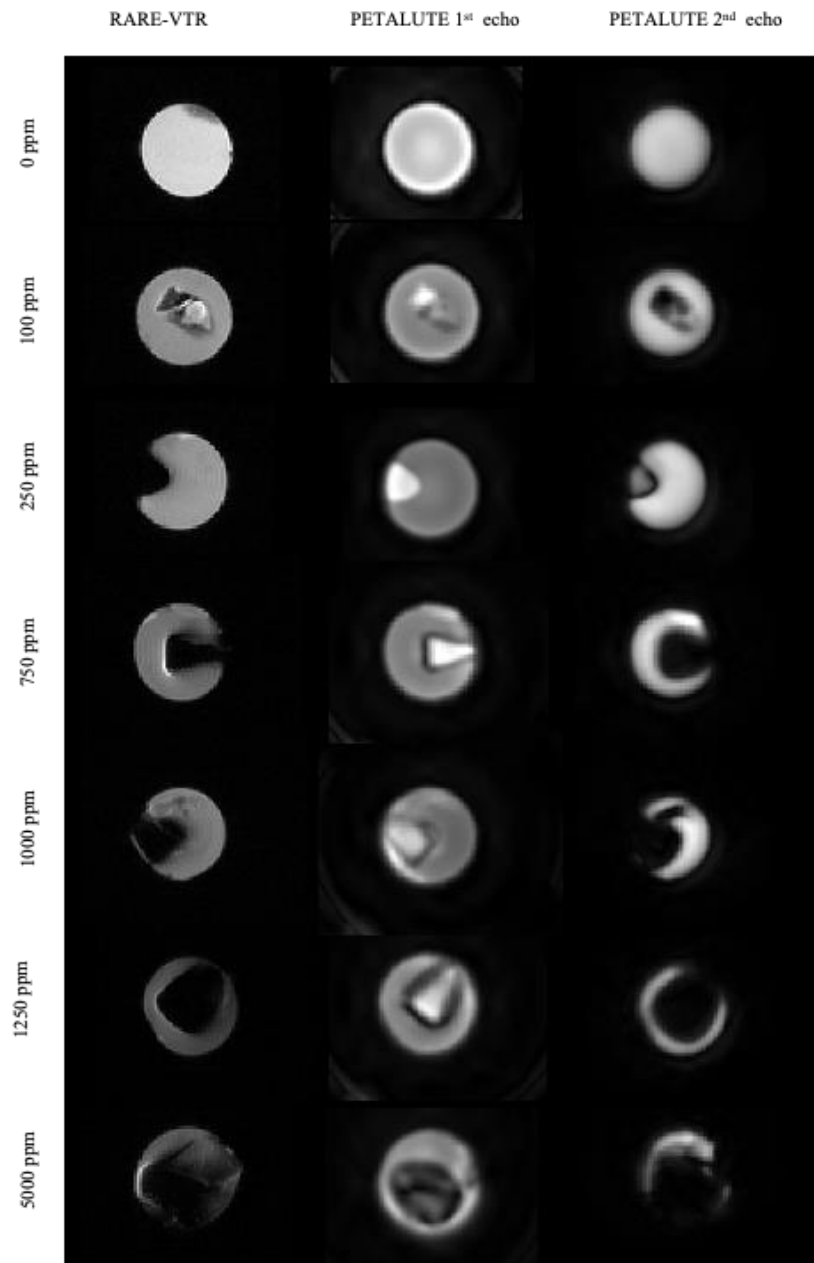


Figure 2. Reconstructed images of phantoms acquired using RARE-VTR and PETALUTE.

Phantom phantoms containing various concentrations of ferumoxytol (0 – 5000 ppm) appear as bright regions in PETALUTE first echo (flip angle = 4) and dark regions in PETALUTE second echo (flip angle = 4) and RARE-VTR images (TR = 934.58 ms).

Table 1. Image protocol parameters

	RARE-VTR	MGE	PETALUTE
Resolution	$0.234 \times 0.234 \times 1 \text{ mm}^3$	$0.234 \times 0.234 \times 1 \text{ mm}^3$	$0.2 \times 0.2 \times 0.2 \text{ mm}^3$
FOV	$30 \times 30 \text{ mm}^3$ 20 slices (thickness = 1 mm)	$30 \times 30 \text{ mm}^3$ 20 slices (thickness = 1 mm)	$40 \times 40 \times 40 \text{ mm}^3$ (Phantom) $60 \times 60 \times 60 \text{ mm}^3$ (In-vivo)
TE	20.3 ms	2 ms, 6 ms, 10 ms, 14 ms, 18 ms, 22 ms, 26 ms, 30 ms, 34 ms, 38 ms	0.016 ms (first echo) 0.032 ms (second echo)
TR	934.58 ms, 1788.44 ms, 2986.55 ms, 5011.78 ms, 15000.0 ms	1500 ms	7 ms
Flip Angle	NA		$4^\circ, 20^\circ$
Acquisition Time	6.18 min	6.4 min	1.08 min/flip-angle (Phantom) 4.31 min/flip-angle (In-vivo)

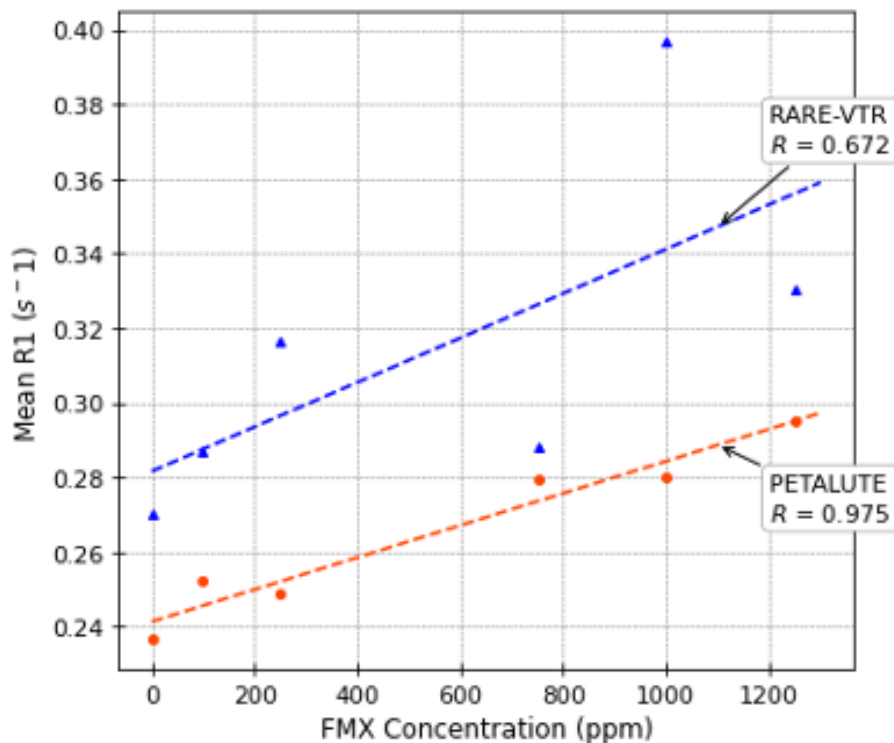


Figure 3. Linear regression of mean R_1 versus ferumoxytol (FMX) concentration for PETALUTE (circles) and RARE-VTR (triangles). The R values were 0.975 for PETALUTE and 0.672 for RARE-VTR. Data at 5000 ppm were excluded as outliers due to extreme artifacts in both methods.

Table 2. Summary of T_1 and R_1 for each ferumoxytol (FMX) phantom measured using RARE-VTR and PETALUTE methods. Data are presented as mean \pm standard deviation (SD).

FMX Concentration (ppm)	RARE-VTR R_1^1 Mean \pm SD (s^{-1})	PETALUTE R_1^1 Mean \pm SD (s^{-1})	RARE-VTR T_1^1 Mean \pm SD (ms)	PETALUTE T_1^1 Mean \pm SD (ms)
0	0.270 ± 0.008	0.237 ± 0.002	3703 ± 103	4229 ± 41
100	0.287 ± 0.038	0.252 ± 0.014	3534 ± 427	3978 ± 237
250	0.316 ± 0.104	0.249 ± 0.002	4170 ± 3874	4008 ± 31
750	0.288 ± 0.126	0.279 ± 0.004	4126 ± 1782	3581 ± 49
1000	0.397 ± 0.184	0.280 ± 0.005	2876 ± 949	3574 ± 58
1250	0.331 ± 0.255	0.295 ± 0.006	5166 ± 4659	3387 ± 69
5000	0.826 ± 0.448	0.270 ± 0.011	1639 ± 983	3706 ± 160

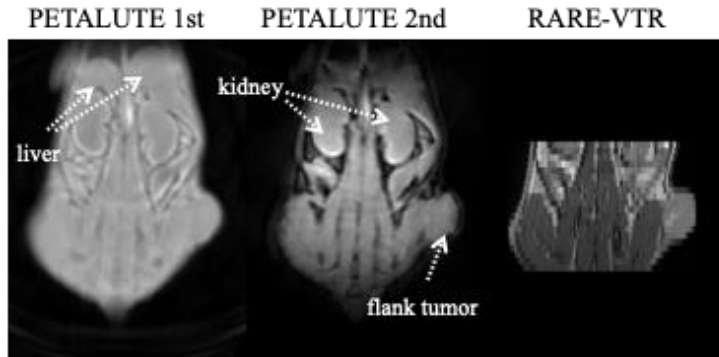


Figure 4. Exemplary coronal images from a control mouse (MS47) acquired using PETALUTE first echo and second echo ($FA = 4^\circ$) and RARE-VTR ($TR = 934.58$ ms).

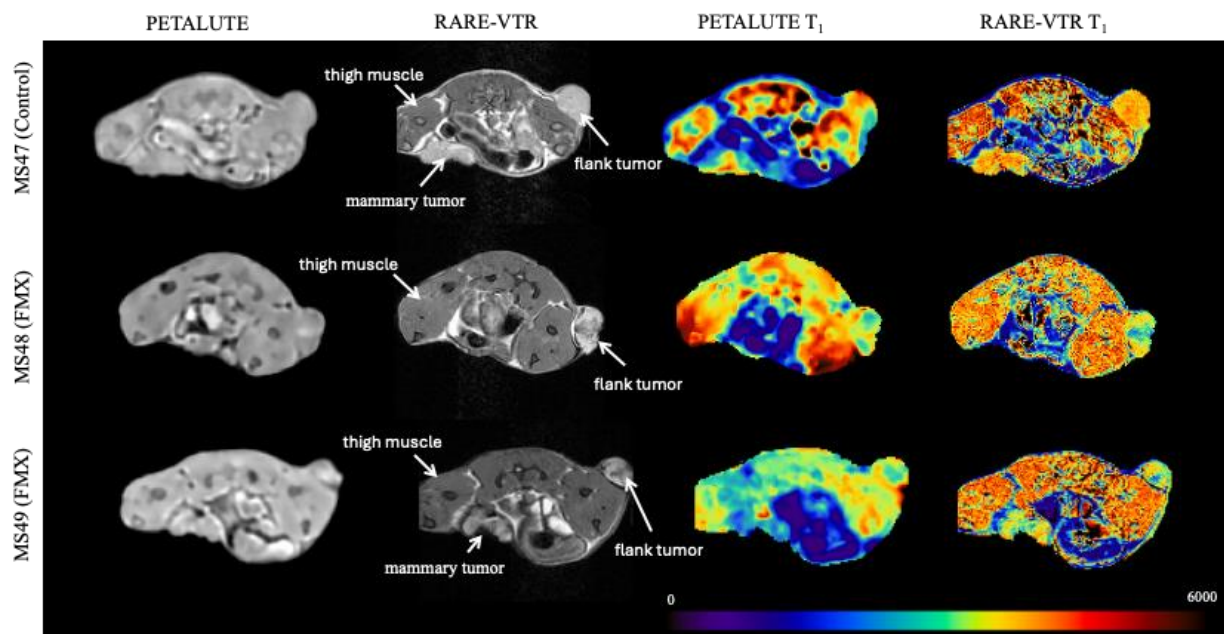


Figure 5. PETALUTE and RARE-VTR images and corresponding T_1 maps from the control mouse (MS47) and the mice with ferumoxytol (FMX) injection (MS48 and MS49). PETALUTE images are first echo acquired with a flip angle of 4° , while RARE-VTR images are acquired with $TR = 934.58$ ms. Thigh muscle, flank tumors and mammary tumors are indicated (the mammary tumor of MS48 appears in a different slice and is not shown here). Color maps show T_1 values in milliseconds, with a scale range of 0–6000 ms.

Table 3. Mean and standard deviation (SD) of T_1 and R_1 values within the ROIs of thigh muscle, flank tumors and mammary tumors in three mice.

ID	Group	ROI	RARE-VTR R_1 Mean \pm SD (s^{-1})	PETALUTE R_1 Mean \pm SD (s^{-1})	RARE-VTR T_1 Mean \pm SD (ms)	PETALUTE T_1 Mean \pm SD (ms)
MS 47	Control	Thigh Muscle	0.242 \pm 0.023	0.247 \pm 0.015	4164 \pm 392	4063 \pm 249
		Flank Tumor	0.260 \pm 0.012	0.298 \pm 0.043	3850 \pm 184	3424 \pm 464
		Mammary Tumor	0.265 \pm 0.029	0.374 \pm 0.063	3821 \pm 396	2745 \pm 443
MS 48	Ferumoxytol	Thigh Muscle	0.258 \pm 0.029	0.240 \pm 0.021	3919 \pm 427	4203 \pm 357
		Flank Tumor	0.295 \pm 0.037	0.318 \pm 0.042	3438 \pm 389	3198 \pm 416
		Mammary Tumor	0.302 \pm 0.073	0.265 \pm 0.048	3472 \pm 691	3894 \pm 667
MS 49	Ferumoxytol	Thigh Muscle	0.239 \pm 0.029	0.251 \pm 0.020	4252 \pm 545	4002 \pm 322
		Flank Tumor	0.306 \pm 0.060	0.307 \pm 0.030	3369 \pm 556	3286 \pm 341
		Mammary Tumor	0.302 \pm 0.060	0.386 \pm 0.049	3401 \pm 500	2632 \pm 330

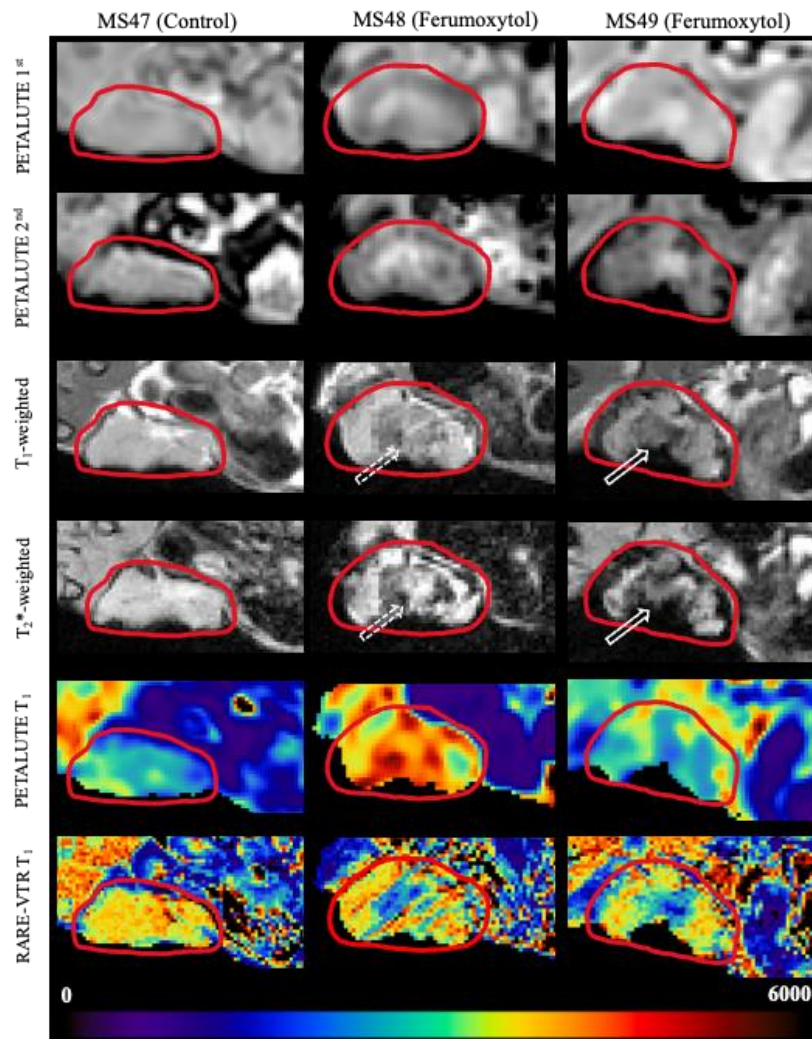


Figure 6. Multimodal images of three included animals focusing on the mammary tumor. Shown are PETALUTE first echo, PETALUTE second echo, T_1 -weighted (RARE-VTR, TE = 20 ms, TR = 933 ms), T_2^* -weighted (MGE, TE = 6 ms, TR = 1500 ms), PETALUTE T_1 map, and RARE-VTR T_1 map images. Mammary tumors are contoured in red. Dashed arrows indicate T_1 hypointensity with persistent T_2^* signal indicated in MS48 while solid arrows indicate T_1 hypointensity with T_2^* signal loss in MS49. MS47 (control) showed uniform intratumor intensity. Color maps display T_1 values in milliseconds, with a scale range of 0–6000 ms.

References

1. Mitchell MJ, Billingsley MM, Haley RM, Wechsler ME, Peppas NA, Langer R. Engineering precision nanoparticles for drug delivery. *Nat Rev Drug Discov.* 2021;20(2):101-124. doi:10.1038/s41573-020-0090-8
2. Blanco E, Shen H, Ferrari M. Principles of nanoparticle design for overcoming biological barriers to drug delivery. *Nat Biotechnol.* 2015;33(9):941-951. doi:10.1038/nbt.3330
3. Wilhelm S, Tavares AJ, Dai Q, et al. Analysis of nanoparticle delivery to tumours. *Nat Rev Mater.* 2016;1(5):16014. doi:10.1038/natrevmats.2016.14
4. Ng TSC, Garlin MA, Weissleder R, Miller MA. Improving nanotherapy delivery and action through image-guided systems pharmacology. *Theranostics.* 2020;10(3):968-997. doi:10.7150/thno.37215
5. Chang DY, Speth JP, Scarpelli ML. Evaluating the theranostic potential of ferumoxytol when combined with radiotherapy in a mammary dual tumor mouse model. *Medical Physics.* 2025;52(7):e17888. doi:10.1002/mp.17888
6. Dennahy IS, Han Z, MacCuaig WM, et al. Nanotheranostics for Image-Guided Cancer Treatment. *Pharmaceutics.* 2022;14(5):917. doi:10.3390/pharmaceutics14050917
7. Fan D, Cao Y, Cao M, Wang Y, Cao Y, Gong T. Nanomedicine in cancer therapy. *Sig Transduct Target Ther.* 2023;8(1):293. doi:10.1038/s41392-023-01536-y
8. Lapusan R, Borlan R, Focsan M. Advancing MRI with magnetic nanoparticles: a comprehensive review of translational research and clinical trials. *Nanoscale Advances.* 2024;6(9):2234-2259. doi:10.1039/D3NA01064C
9. Girard OM, Du J, Agemy L, et al. Optimization of iron oxide nanoparticle detection using ultrashort echo time pulse sequences: Comparison of T_1 , T_2^* , and synergistic $T_1 - T_2^*$ contrast mechanisms: IONP Detection Using UTE Sequences. *Magn Reson Med.* 2011;65(6):1649-1660. doi:10.1002/mrm.22755
10. Jeon M, Halbert MV, Stephen ZR, Zhang M. Iron Oxide Nanoparticles as T1 Contrast Agents for Magnetic Resonance Imaging: Fundamentals, Challenges, Applications, and Prospectives. *Advanced Materials.* 2021;33(23):1906539. doi:10.1002/adma.201906539
11. Rahman M. Magnetic Resonance Imaging and Iron-oxide Nanoparticles in the era of Personalized Medicine. *Nanotheranostics.* 2023;7(4):424-449. doi:10.7150/ntno.86467
12. Weiskopf N, Edwards LJ, Helms G, Mohammadi S, Kirilina E. Quantitative magnetic resonance imaging of brain anatomy and in vivo histology. *Nat Rev Phys.* 2021;3(8):570-588. doi:10.1038/s42254-021-00326-1
13. Bottomley PA, Foster TH, Argersinger RE, Pfeifer LM. A review of normal tissue hydrogen NMR relaxation times and relaxation mechanisms from 1–100 MHz: Dependence on tissue type, NMR frequency, temperature, species, excision, and age. *Medical Physics.* 1984;11(4):425-448. doi:10.1118/1.595535

14. Messroghli DR, Moon JC, Ferreira VM, et al. Clinical recommendations for cardiovascular magnetic resonance mapping of T1, T2, T2* and extracellular volume: A consensus statement by the Society for Cardiovascular Magnetic Resonance (SCMR) endorsed by the European Association for Cardiovascular Imaging (EACVI). *Journal of Cardiovascular Magnetic Resonance*. 2017;19(1):75. doi:10.1186/s12968-017-0389-8
15. Kolb H, Absinta M, Beck ES, et al. 7T MRI Differentiates Remyelinated from Demyelinated Multiple Sclerosis Lesions. *Annals of Neurology*. 2021;90(4):612-626. doi:10.1002/ana.26194
16. Eck BL, Yang M, Elias JJ, et al. Quantitative MRI for Evaluation of Musculoskeletal Disease: Cartilage and Muscle Composition, Joint Inflammation, and Biomechanics in Osteoarthritis. *Investigative Radiology*. 2023;58(1):60. doi:10.1097/RLI.0000000000000909
17. Zhang J, Ring HL, Hurley KR, et al. Quantification and biodistribution of iron oxide nanoparticles in the primary clearance organs of mice using T1 contrast for heating. *Magnetic Resonance in Medicine*. 2017;78(2):702-712. doi:10.1002/mrm.26394
18. Simon GH, Bauer J, Saborovski O, et al. T1 and T2 relaxivity of intracellular and extracellular USPIO at 1.5T and 3T clinical MR scanning. *Eur Radiol*. 2006;16(3):738-745. doi:10.1007/s00330-005-0031-2
19. Zhang L, Zhong X, Wang L, et al. T1-weighted ultrashort echo time method for positive contrast imaging of magnetic nanoparticles and cancer cells bound with the targeted nanoparticles. *J Magn Reson Imaging*. 2011;33(1):194-202. doi:10.1002/jmri.22412
20. Korchinski DJ, Taha M, Yang R, Nathoo N, Dunn JF. Iron Oxide as an MRI Contrast Agent for Cell Tracking: Supplementary Issue. *Magn Reson Imaging Insights*. 2015;8s1:MRI.S23557. doi:10.4137/MRI.S23557
21. Liu W, Dahnke H, Rahmer J, Jordan EK, Frank JA. Ultrashort T2* Relaxometry for Quantitation of Highly Concentrated Superparamagnetic Iron Oxide (SPIO) Nanoparticle Labeled Cells. *Magn Reson Med*. 2009;61(4):761-766. doi:10.1002/mrm.21923
22. Du J, Ma G, Li S, et al. Ultrashort Echo Time (UTE) Magnetic Resonance Imaging of the Short T2 Components in White Matter of the Brain Using a Clinical 3T Scanner. *Neuroimage*. 2014;87:32-41. doi:10.1016/j.neuroimage.2013.10.053
23. Ring HL, Gao Z, Sharma A, et al. Imaging the distribution of iron oxide nanoparticles in hypothermic perfused tissues. *Magnetic Resonance in Medicine*. 2020;83(5):1750-1759. doi:10.1002/mrm.28123
24. Larson PEZ, Gurney PT, Nayak K, Gold GE, Pauly JM, Nishimura DG. Designing Long-T2 Suppression Pulses for Ultrashort Echo Time Imaging. *Magn Reson Med*. 2006;56(1):94-103. doi:10.1002/mrm.20926
25. Gatehouse PD, Bydder GM. Magnetic Resonance Imaging of Short T2 Components in Tissue. *Clinical Radiology*. 2003;58(1):1-19. doi:10.1053/crad.2003.1157
26. Ma YJ, Searleman AC, Jang H, et al. Whole-Brain Myelin Imaging Using 3D Double-Echo Sliding Inversion Recovery Ultrashort Echo Time (DESIRE UTE) MRI. *Radiology*. 2020;294(2):362-374. doi:10.1148/radiol.2019190911

27. Jang H, Ma Y, Carl M, Jerban S, Chang EY, Du J. Ultrashort echo time Cones double echo steady state (UTE-Cones-DESS) for rapid morphological imaging of short T2 tissues. *Magnetic Resonance in Medicine*. 2021;86(2):881-892. doi:10.1002/mrm.28769

28. Shen X, Özen AC, Monsivais H, et al. High-resolution 3D ultra-short echo time MRI with Rosette k-space pattern for brain iron content mapping. *Journal of Trace Elements in Medicine and Biology*. 2023;77:127146. doi:10.1016/j.jtemb.2023.127146

29. Shen X, Özen AC, Sunjar A, et al. Ultra-short T2 components imaging of the whole brain using 3D dual-echo UTE MRI with rosette k-space pattern. *Magnetic Resonance in Medicine*. 2023;89(2):508-521. doi:10.1002/mrm.29451

30. Helms G, Dathe H, Dechent P. Quantitative FLASH MRI at 3T using a rational approximation of the Ernst equation. *Magnetic Resonance in Medicine*. 2008;59(3):667-672. doi:10.1002/mrm.21542

31. Insko EK, Bolinger L. Mapping of the Radiofrequency Field. *Journal of Magnetic Resonance, Series A*. 1993;103(1):82-85. doi:10.1006/jmra.1993.1133

32. Dathe H, Helms G. Exact algebraization of the signal equation of spoiled gradient echo MRI. *Phys Med Biol*. 2010;55(15):4231. doi:10.1088/0031-9155/55/15/003

33. Ishimori Y, Shimanuki T, Kobayashi T, Monma M. Fast B1 Mapping Based on Double-Angle Method with T1 Correction Using Standard Pulse Sequence. *J Med Phys*. 2022;47(1):93-98. doi:10.4103/jmp.jmp_78_21

34. Pieper S, Halle M, Kikinis R. 3D Slicer. In: *2004 2nd IEEE International Symposium on Biomedical Imaging: Nano to Macro (IEEE Cat No. 04EX821)*. 2004:632-635 Vol. 1. doi:10.1109/ISBI.2004.1398617

35. Gillis P, Koenig SH. Transverse relaxation of solvent protons induced by magnetized spheres: Application to ferritin, erythrocytes, and magnetite. *Magnetic Resonance in Medicine*. 1987;5(4):323-345. doi:10.1002/mrm.1910050404

36. Feng Q, Xu X, Wei C, et al. The Dynamic Interactions between Nanoparticles and Macrophages Impact Their Fate in Brain Tumors. *Small*. 2021;17(49):2103600. doi:10.1002/smll.202103600

37. Anderson MA, Knipp DE, Noda Y, et al. MRI-Based Tumor Necrosis Depiction in Pancreatic Ductal Adenocarcinoma: Can It Predict Tumor Aggressiveness? *Cancers*. 2023;15(8):2313. doi:10.3390/cancers15082313

38. Lipka A, Sawiak S, Shen X, et al. Accelerated Preclinical UHF Abdominal T1 Mapping Using Novel Rosette Ultrashort Echo Time (PETALUTE).; 2024. doi:10.58530/2024/0575

39. Liu S, Brisset JC, Hu J, Haacke EM, Ge Y. Susceptibility weighted imaging and quantitative susceptibility mapping of the cerebral vasculature using ferumoxytol. *Journal of Magnetic Resonance Imaging*. 2018;47(3):621-633. doi:10.1002/jmri.25809